Transactions of Materials Research 1 (2025) 100004

Contents lists available at ScienceDirect

Transactions of Materials Research

journal homepage: www.sciencedirect.com/journal/transactions-of-materials-research

Enhanced photocatalytic and spintronic properties in proposed α-MXene family via ferroelectric effect

Yinggan Zhang [a,b], Zhou Cui [c], Baisheng Sa [c], Jian Zhou [a], Zhimei Sun [a,*]

[a] School of Materials Science and Engineering, Beihang University, Beijing, 100191, China
[b] College of Materials, Xiamen Key Laboratory of Electronic Ceramic Materials and Devices, Fujian Provincial Key Laboratory of Theoretical and Computational Chemistry, Xiamen University, Xiamen, 361005, China
[c] Multiscale Computational Materials Facility & Materials Genome Institute, School of Materials Science and Engineering, Fuzhou University, Fuzhou, 350108, China

ARTICLE INFO

Keywords:
First-principles calculation
Ferroelectric photocatalysis
Spintronics

ABSTRACT

Two-dimensional transition metal carbides (MXenes) have garnered significant attention due to their distinctive physical and chemical properties. In this study, utilizing density functional theory calculations, we introduce a novel phase of transition metal carbide with the space group of *R*3*m*, designated as α-MXene with the chemical formula M_2CX_2 (M = Ti, Zr, Hf, V, Nb, Ta, Cr, Mo, W, Mn; X = O, F). Notably, α-MXene possesses an ABBCA atomic layer configuration closely resembles the two-dimensional ferroelectric material α-In_2Se_3, distinct from the close packing ABCAB atomic stacking observed in typical MXenes. It is highlighted that α-MXene exhibits adjustable ferroelectric properties with moderate polarization reversal energy barriers, including five rare ferroelectric metals and one Dirac-semimetal. Moreover, α-MXenes not only enable photocatalytic reactions by utilizing infrared light to overcome the band gap restriction of 1.23 eV, but also generate hydrogen and oxygen gases on separate surfaces due to electric field induced by ferroelectric effect. Additionally, ferroelectric tunnel junctions (FTJs) based on α-MXene show exceptionally high tunneling electroresistance ratios (TERs), indicating their suitability for advanced ferroelectric memory device applications. Our research provides a viable strategy for exploring ferroelectric materials within the expansive MXene family and exemplifies the applications of α-MXenes in photocatalysis and spintronics.

1. Introduction

Two-dimensional (2D) materials have exhibited unique physical and chemical properties due to the reduction in both dimension and size [1]. In recent years, as significant advances have been made in synthetic techniques, an increasing number of 2D materials have been successfully realized [2]. Among them, 2D transition metal carbide (MXene) has emerged as a rapidly rising star, formed through the selective chemical etching of A from the parent MAX phase, where M represents transition metal atoms, A represents an IIA or IVA element, and X denotes carbon or nitrogen [3–8]. Consequently, MXenes are typically constituted of X monolayer sandwiched between metal M layers, terminated by oxygen and/or fluorine surface functionalized groups. A wide variety of chemical compositions in MXenes endow them with a plethora of fascinating electronic, magnetic, and electrochemical properties [6]. Thus, MXenes have been actively investigated for various applications including electronics, optoelectronics, photocatalysts, and battery anodes [9–13]. Notably, MXene Sc_2CO_2 prefers a ferroelectric ground state with the asymmetrical O surface groups, holding great promise for applications in nanoelectronics and photovoltaics [14]. Additionally, based on high-throughput screening, more asymmetrical surface functionalized MXenes have been proposed as ferroelectric materials [15,16]. Since typical MXenes exhibit centrally symmetric 2D structures, ferroelectricity mainly originates from the asymmetry surface functional groups. This ferroelectricity, however, tends to be weak and challenging to sustain [11,17–19]. Therefore, identifying additional ferroelectric phases in MXenes remains a significant challenge and is a demanding area of great interest.

There are two well-established layered phases of the In_2Se_3 crystalline structure, named as α-In_2Se_3 and β-In_2Se_3. Coincidentally, the typical MXenes phase can be regarded as atomic stacking configurations according to β-In_2Se_3, where both indium atoms have octahedral bonding configurations in the five alternating Se-In-Se-In-Se quintuple layers with ABCAB atomic configurations. On the other hand, in α-In_2Se_3, the

* Corresponding author.
E-mail address: zmsun@buaa.edu.cn (Z. Sun).

https://doi.org/10.1016/j.tramat.2025.100004
Received 21 March 2025; Received in revised form 31 March 2025; Accepted 31 March 2025
Available online 2 April 2025

quintuple layers show different ABBCA atomic configurations, where two indium atoms are placed in different chemical coordinate environments: one indium atom has a tetrahedral bonding arrangement with four selenide atoms, and the other indium atom is bonded octahedrally to six selenide atoms [20,21]. It is noteworthy that α-In_2Se_3 is the stable phase with intrinsic ferroelectric properties due to the asymmetric atomic arrangement, which have been theoretically and experimentally observed [22,23]. The spontaneous polarization makes it promising for non-volatile memory device like ferroelectric random-access memory (FeRAM) and ferroelectric tunnel junctions (FTJs) [21]. The ferroelectricity of α-In_2Se_3 could also be integrated with spintronics, thus could be critical in the design of high-efficiency spin storage and spin transport devices by controlling spin currents [21,24]. Moreover, α-In_2Se_3 can be utilized as a semiconductor material in field-effect transistors (FETs), and the ferroelectric properties broaden functionality, allowing the design of low-power, programmable transistors [24,25]. It is noted that α-In_2Se_3 remains stable at ambient conditions below 473 K, above this temperature, α-In_2Se_3 transforms to β-In_2Se_3 [21]. An interesting idea come to our mind: if MXenes follow the atomic configuration of α-In_2Se_3, can be named as α-MXenes, the fascinating intrinsic ferroelectric characters will be anticipated due to the asymmetry 2D atomic structure nature. Therefore, a thorough and in-depth investigation of α-MXenes is imperative, allowing the comprehend of their physical performances and rational design of devices for various applications.

In this work, we predict a new phase for M_2CX_2 MXenes (termed α-MXenes) by first-principles calculations, where M stands for Ti, Zr, Hf, V, Nb, Ta, Cr, Mo, W, Mn with X is O or F. The lattice dynamical stability of α-MXenes has been confirmed by phonon calculations. Moreover, the computed formation energies of α-MXenes are more negative than those of α-In_2Se_3 monolayers. Furthermore, a tunable electric polarization can be achieved in these diverse α-MXenes. It is highlighted that three α-MXenes are highly efficient ferroelectric photocatalysts utilizing solar energy from visible to infrared light with effective separation of photogenerated electrons and holes. In addition, FTJs based on α-MXenes demonstrate excellent performance from atomic device simulations. Our study presents a practical method for investigating ferroelectric materials in the broad MXene family and highlights the application prospects of α-MXenes in photocatalysis and spintronics.

2. Computational details

Density functional theory calculations were implemented in Vienna *ab initio* simulation package (VASP) based on density functional theory (DFT) [26,27]. The structures of two-dimensional monolayers and heterostructures were built by the ALKEMIE platform [28,29]. The Perdew-Burke-Ernzerhof (PBE) functional of generalized-gradient approximation (GGA) was employed to deal with the exchange-correlation potential [30]. The energy cutoff was set to 500 eV, and the *k*-point sampling grid was set to 12 × 12 × 1 for the structure optimization and self-consistent calculations. The vacuum space of 20 Å was inserted along the *z*-direction to avoid the interaction of adjacent layers. The energy and force convergence criterions were set as 1×10^{-5} eV. The dipole correction was considered to avoid the effect of the vacuum electric field [31]. Time-dependent Hartree-Fock (TDHF) [32] calculations on the base of HSE06 [33] were applied to obtain precise absorption coefficient. The PHONOPY code based on force constants gotten by the VASP-DFPT (density-functional perturbation theory) interface [34,35] was employed to explore the dynamic stability, and a 7 × 7 × 1 supercell with *k*-point mesh of 3 × 3 × 1 was adopted in the calculations.

The transmission properties of the devices were carried out based on the non-equilibrium Green's function (NEGF) method as implemented in the QuantumWise Atomistix ToolKit (QuantumATK) package [36,37]. The GGA-PBE functional with a linear combination of atomic orbitals (LCAO) norm-conserving PseudoDojo pseudopotential [38] was employed to deal with the electron exchange and correctional interactions. The valence electrons are expanded in a numerical atomic-orbital basis set of double-zeta polarization (DZP) for all atoms [39]. The cutoff energy was set to 125 Hartree, and the convergence criterion of the force was set to 0.01 eV/Å. The Monkhorst *k*-point meshes are set to 8 × 1 × 1 and 8 × 1 × 165 for the central scattering regions and electrodes. A denser 121 × 1 *k*-point mesh was employed in the spin-dependent transmission calculations of FTJs.

3. Results and discussion

3.1. Structure and stability of α-MXene

It is well known that bulk In_2Se_3 exists in α and β layered crystalline phases, which are bonded by the corresponding 2D In_2Se_3 via weak van der Waals (vdW) forces [20]. As illustrated in Fig. S1, the 2D α-In_2Se_3 with ABBCA atomic configurations is more stable than β-In_2Se_3 with ABCAB atomic configurations [20,22,24,40]. Fig. 1c illustrates the top view of atoms along the vertical direction in one of the triangular lattices. The relative atomic coordinates of A, B, and C are (1/3, 1/3, *z*), (2/3, 2/3, *z*), and (0, 0, *z*), respectively. As is seen, the β-In_2Se_3 belongs to face-centered cubic (fcc) crystal structures, and they are the metastable phase of In_2Se_3. Note that in fcc structures, the two surface Se atoms separately align with In atoms in the opposite side, whereas the central Se atoms are hexagonally coordinated by the neighboring six In atoms. Interestingly, the atomic arrangements of this metastable β-In_2Se_3 structures are in accord with 2D MXenes (referred to as β-MXene), as displayed in Fig. 1a. On this occasion, the prototypical β-In_2Se_3 quintuple atomic layer Se-In-Se-In-Se turns out to be X-M-C-M-X atomic arrangement in β-MXene. Spontaneously, MXene with the α-In_2Se_3 atomic configurations (called α-MXene) is presented in Fig. 1b. Similarly to α-In_2Se_3, in a five-layer α-MXene structure, the third central C atoms is tetrahedrally coordinated by the second and fourth M atoms with the space group of *R3m*. In the tetrahedron, one M − C bond is along the negative *c*-axis vertically with the other three bonds along the *c*-axis angularly. While the X atoms in the first and fifth layers are located on the hollow sites of second and fourth layers, respectively. In consequence, the atomic spacing of the third central C layer and the second and fourth M layers in the tetrahedron break the mirror symmetry of α-MXene. This is dramatically different from the centrosymmetric β-MXene, and makes α-MXene endow with the emergence of the spontaneous out-of-plane electric polarization.

In the present work, we mainly focus on carbide α-MXenes with M elements including Ti, Zr, Hf, V, Nb, Ta, Cr, Mo, W, and Mn, and terminating surface groups of O and F, as presented in Fig. 2a. Firstly, we have calculated the lattice parameters using the PBE method. The results are summarized in Fig. 1d, from which one can see that the optimized lattice constants of F surface groups α-MXene are smaller than those with O surface groups, except for the Mo and W-based α-MXene. Moreover, Table S1 illustrates the lattice parameters of β-MXene. Apparently, for the majority of the investigated MXenes, the α-MXene phases have smaller lattice parameters than β-MXene. Such results are consistent with the fact that the lattice constants of β-In_2Se_3 (3.981 Å) are slightly smaller than that of α-In_2Se_3 (4.106 Å), as estimated by our calculations and previous research [20].

In addition, the formation energy (E_{form}) was calculated to evaluate the stability of α-MXene, which is defined by the following equation according previous works [17,41,42]:

$$E_{form} = (E_{M_2CX_2} - \mu_M - \mu_C - \mu_x) / 5, \quad (1)$$

where $E_{M_2CX_2}$ stands for the total energy of α-MXene M_2CX_2, and the chemical potentials μ_M, μ_C, μ_X are respectively taken from transition metal M crystal, graphite, and O_2/F_2 molecule, respectively. The results are displayed in Fig. 2b and c, with the formation energies of successfully fabricated 2D α-In_2Se_3 and $CrGeTe_3$ included as references. Generally, for both O and F surface groups, IVB group α-MXenes show the lowest E_{form}

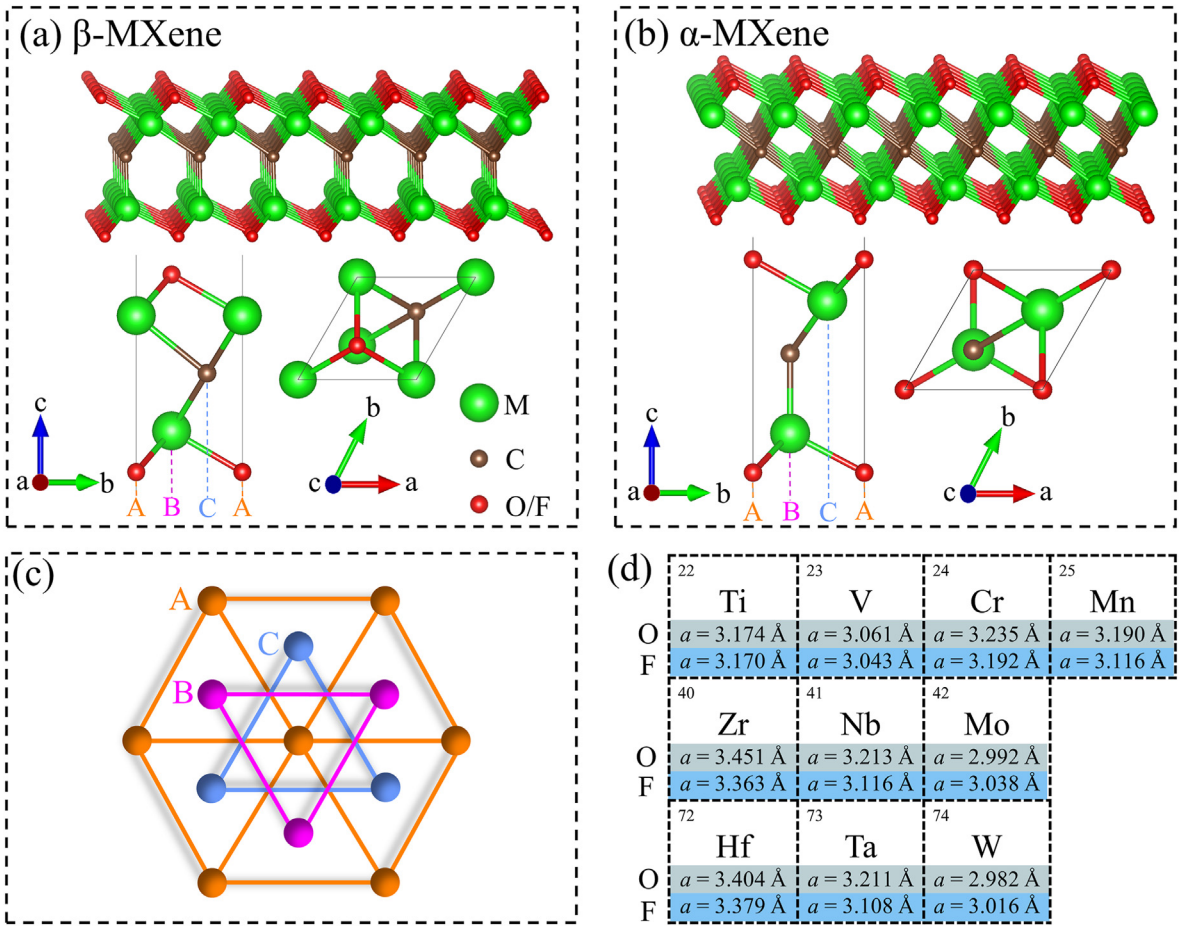

Fig. 1. Structure of α-MXene. The atomic configurations of (a) β-MXene and (b) α-MXene. (c) The structure along the vertical direction with the atoms arranged in one of the triangular lattices A, B or C. (d) Calculated lattice parameters of *a* (Å) for α-MXene in different M atoms in the periodic table and O/F terminated surface groups.

and VIB group α-MXenes exhibit relatively higher E_{form}. It is obviously seen that the E_{form} of all investigated α-MXenes are more negative than that of α-In_2Se_3 monolayers. In comparison to 2D $CrGeTe_3$, only the formation energy of W_2CF_2 is slightly greater than that of 2D $CrGeTe_3$ among the explored 20 α-MXenes. Furthermore, the calculated phonon band structures including 3 acoustic and 12 optical branches (15 branches in total) for all explored α-MXenes have been illustrated in Fig. 2d and e, and Figs. S2 and S3. All frequencies in the phonon dispersion curves are positive, confirming the dynamic stability of α-MXenes. As is discussed, the evaluated thermodynamic and lattice dynamic stabilities of α-MXenes provide a fundamental basis for future experimental fabrication.

3.2. *Ferroelectric and distinctive physical characteristics of α-MXene*

As studied above, due to the crystal centrosymmetric breaking, α-MXenes are promisingly characterized with ferroelectric nature. We have firstly reproduced the magnitudes of the electric dipoles for α-In_2Se_3, the estimated value by the PBE method is 0.093 eÅ, and 0.111 eÅ according to the HSE06 approach. Such magnitudes are in excellent agreement with the previous DFT results, with the values of 0.094 eÅ and 0.11 eÅ by the PBE and HSE06 approach [20]. The calculated electric polarizations of α-MXenes by PBE approach are listed in the top-left panel of Fig. 3. Herein, α-MXenes exhibit a regulable electric polarization from 0.008 eÅ to 0.156 eÅ benefiting by the various kinds of MXenes. In detail, for IVB groups, the O functionalized MXenes show higher magnitudes of electric dipoles, while the VIB groups exhibit an opposite tendency, as the F functionalized MXenes possess higher electric polarization. We have estimated the electric polarization by the HSE06 approach as well and the results are summed up in Table S2. Note that for all the explored α-MXene, the HSE06 method provides higher electric polarization than PBE, in line with previous work [20]. However, the differences are slightly and acceptable.

The ability to reverse electric polarization is essential for ferroelectric materials to be useful in practical applications [20]. Therefore, we turn to the kinetic pathways and corresponding activation energies for switching the polarization direction in α-MXenes. The non-polar symmetric transition state (TS) and the polarization-reversing process are illustrated in Fig. 3. The C atoms in the central layer occupy B sites aligned vertically with the lower transition metal layer, causing the electric dipole to point downward. In transformation process, these C atoms shift to adjacent C sites aligned with the upper transition metal layer, resulting in a reversal of the electric dipole direction. The activation energy barriers are summed up in the top-right panel of Fig. 3. Note that the energy barrier of α-In_2Se_3 during the polarization reversal process is 1.01 eV by our calculations, which is close to the value of previous work [20]. As shown in Fig. 3, all the F terminated MXenes have a higher energy barrier than the corresponding O terminated MXenes. Note that W_2CO_2 exhibits the lowest energy barrier at 0.496 eV, while Hf_2CF_2 has the highest at 1.941 eV. This range highlights the variability in energy barriers across these ferroelectric materials. Clearly, the energy barriers of these structures are compared with that of α-In_2Se_3, which has been successfully fabricated in experiments [40]. Thus, α-MXene has great potential to be experimentally synthesized and to put into practical use in the near future.

It is well known that traditional β-MXenes exhibit a diverse range of electronic properties, including metallicity, semiconductivity, and non-conductivity. Because of the similar crystal structure, we propose that our designed new structure α-MXene will endow with various electronic

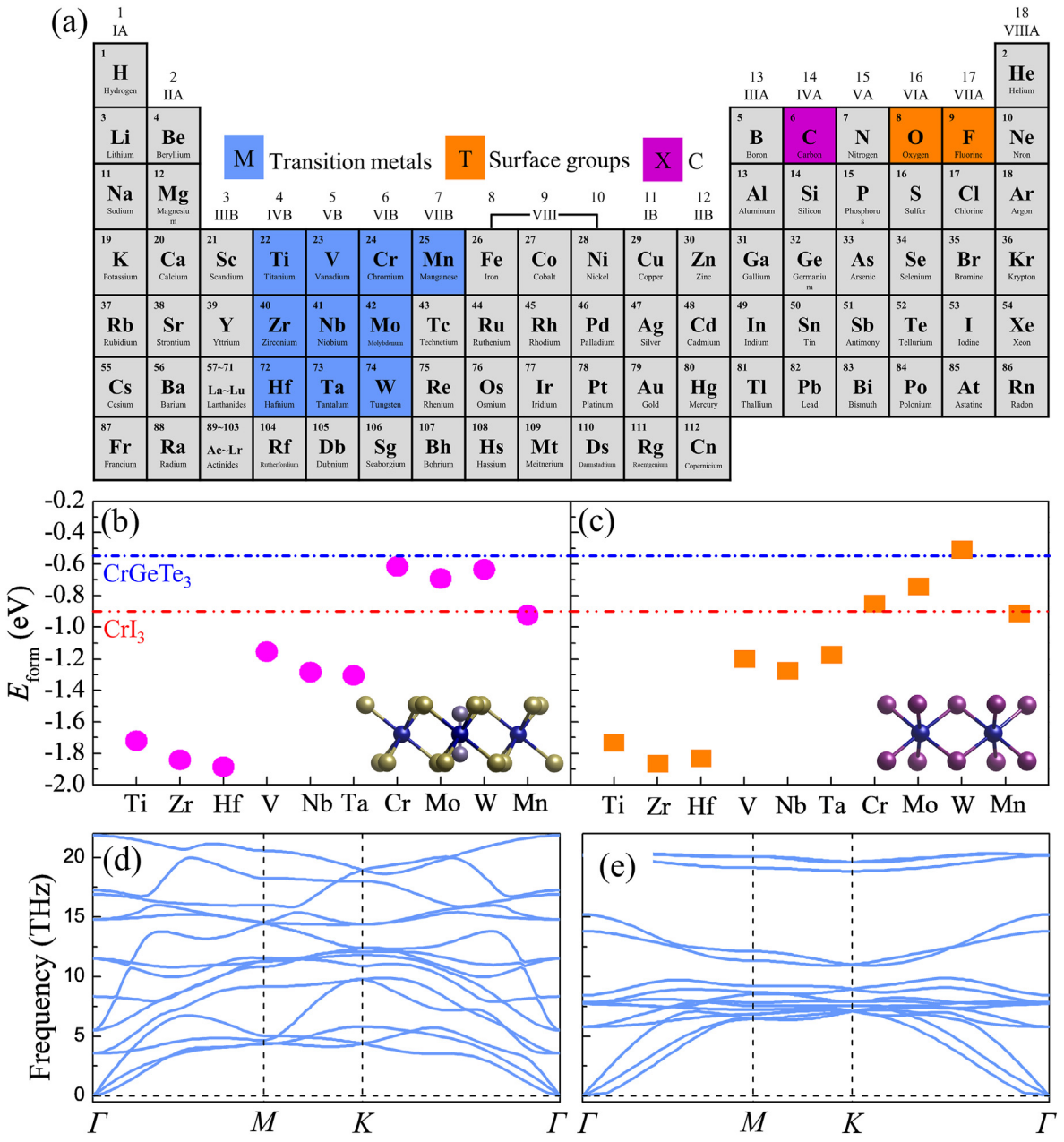

Fig. 2. Stability of α-MXene. (a) Chemical compositions of α-MXenes in the periodic table. Calculated formation energies of α-MXene with (b) O-terminated surface group (c) and F-terminated surface group. In (b) and (c), the blue and red dashed dot lines represent the formation energies of $CrGeTe_3$ and CrI_3 monolayers, respectively, and the inset structures are the side views of $CrGeTe_3$ and CrI_3, respectively. Phonon dispersion curves for (d) Ti_2CO_2 and (e) Ti_2CF_2 α-MXenes.

properties. We have then calculated the total and partial density of states (DOS) and band gaps in Fig. 4. As is seen, eight semiconductors have been found with band gaps ranging from 0.48 eV to 1.36 eV, including six IVB-group α-MXenes, added with Nb_2CO_2 and Ta_2CO_2. Moreover, in these eight semiconducting α-MXenes, only Nb_2CO_2 are characterized with direct band gaps, both the conduction band minimum (CBM) valence and band maximum (VBM) are located at Gamma points, as displayed in Fig. S4. Deeply, for all the semiconductors, both the CBM and VBM are predominantly dominated by the *d* states from the transition metal atoms. It is worth mentioning that, for the O-functionalized α-MXenes in IVB groups, the VBM are occupied by the 2*p* states from C and O atoms as well. Beyond that, for all the investigated α-MXenes, 2*p* electrons from the third layers C atoms are strongly hybridized with the *d* electrons from the second- and fourth-layer transition metal atoms. Moreover, the *d* electrons also hybridize with the 2*p* electrons from top and bottom layers O or F atoms, suggesting the strong covalent bonds between them, which is very similar to β-MXenes [18,19]. Furthermore, our results demonstrate that V_2CX_2, Cr_2CX_2, and Mn_2CX_2 α-MXenes (X = O or F) exhibit ferromagnetic properties, with the total magnetic moment of 1.832μ_B, 3.975μ_B, and 5.854μ_B per unit cell, respectively. However, when utilized as polar materials for device application, these three systems may exhibit complex magnetic interactions, thereby impeding high-density integration in nanodevices [43,44]. Consequently, we will not explore these three ferromagnetic α-MXenes in the following discussion.

Especially, as displayed in Fig. 4, the band gap of W_2CO_2 is 0 eV, which is distinct from other α-MXenes. We have further calculated the band structure of W_2CO_2 in Fig. 5a and b to gain a deeper understanding of the electronic properties. As seen from Fig. 5a, the bands mainly from transition metal atom W barely cross Fermi level, inducing to a semi-metallic character. The three-dimensional band profiles are illustrated

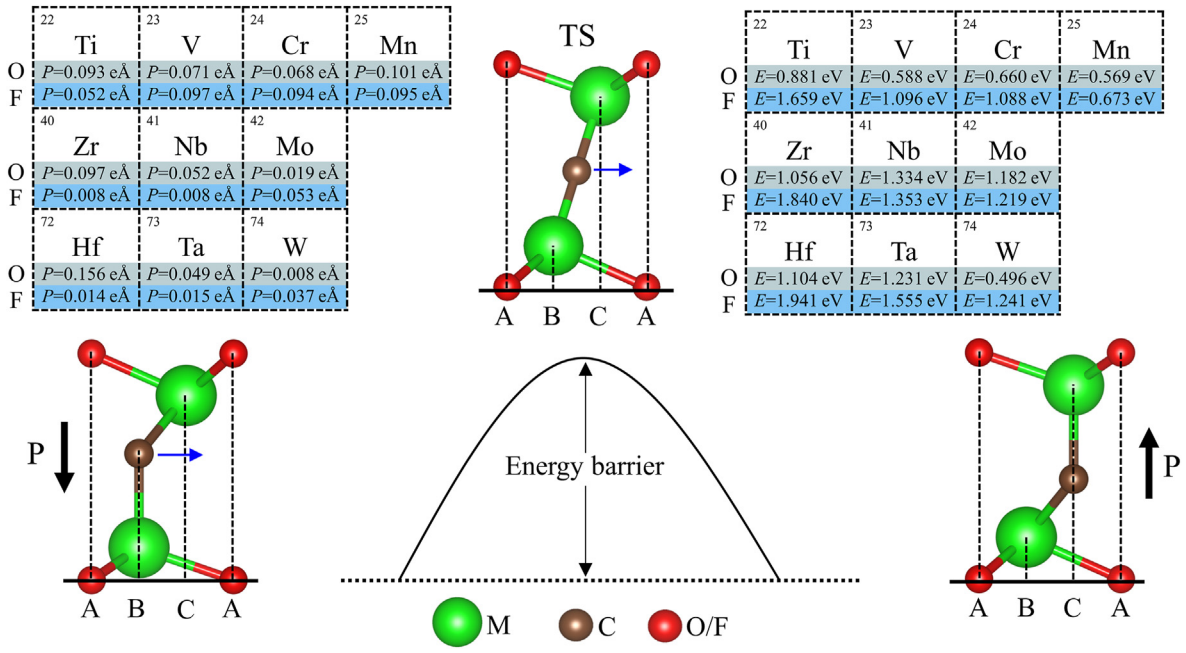

Fig. 3. Ferroelectric properties of α-MXene. Polarization reversal processes from ferroelectric phase with the electric polarization pointing downward (left) to the ferroelectric phase with the electric polarization pointing upward (right). The top-left panel is the calculated electric polarization (eÅ) of α-MXene obtained by the PBE approach. The top-right panel is the estimated polarization-reversing energy barriers (eV).

in Fig. 5b as well. Different from β-MXene $Hf_3C_2O_2$, for another semimetal proposed by Zha et al. [45], its VBM is situated at the Γ point, while the CBM is determined at another high-symmetry point (M point). For the explored W_2CO_2, both the CBM and VBM located at the same high-symmetry point Γ. Such CBM and VBM touch each other on the Fermi level, leading to the so-called Dirac cone, which can induce breathtaking properties, such as ultra-high Fermi velocity, exceedingly high carrier mobility, fast charge transport, and zero effective mass of the carriers [46–48]. Hence, W_2CO_2 α-MXene may serve as a significant Dirac material for the development of high-speed, low-dissipation devices due to its intrinsic Dirac-semimetal nature.

Moreover, we found that Nb_2CF_2, Ta_2CF_2, Mo_2CO_2, Mo_2CF_2, and W_2CF_2 α-MXenes are ferroelectric metal, as the Fermi level is across by the d states from the transition metal atoms with the intrinsic ferroelectricity of them. Ferroelectric metal is first proposed by Anderson and Blount in 1965 [49]. Traditionally, ferroelectricity and metallicity were thought to be mutually exclusive because metals have free electrons that screen any internal electric fields, preventing the establishment of the electric dipoles necessary for ferroelectric behavior. In ferroelectric metals, the free electrons do not screen the internal dipoles completely, enabling spontaneous polarization to persist despite the presence of mobile charge carriers. This incomplete screening allows the structure to maintain its polarized state, which is essential for ferroelectric behavior [49]. Ferroelectric metals offer significant potential for a range of advanced electronic applications, including memory storage devices, where they could integrate the advantages of ferroelectric switching with the electrical conductivity of metals. Additionally, these materials are gaining interest for their possible roles in cutting-edge technologies such as quantum computing and next-generation transistors [50,51]. Polar metal WTe_2 has demonstrated spontaneous electric polarization that can be switched by applying an external electric field, potentially marking the first experimental observation of the coexistence of ferroelectricity and metallicity in a 2D material [52]. Nevertheless, until now, examples of ferroelectric metals remain exceedingly rare [50]. In our study, we have revealed five ferroelectric metals in α-MXenes. The coexistence of ferroelectricity and metallicity in these materials can be explained as follows. Taking Mo_2CF_2 as an example, the partial electron density of Mo_2CF_2 within an energy range of ±0.05 eV around the Fermi level is plotted in Fig. 5c. Surprisingly, the electron density mainly concentrated on the lower surface. We have then visualized the electron density by integrating it over the x-y plane, defined as conducting electron density, which has successfully clarified the ferroelectricity in 2D metal systems in previous work [53]. The integration over the x-y plane of charge density difference between ferroelectric and paraelectric phases are referred as polarizing electron density. The electron density of paraelectric phases make no contribution to polarization of the system, polarizing electron density can reflect the electronic contribution to the polarization. The conducting and polarizing electron density are displayed in Fig. 5d. Clearly, the polarizing electron density is distributed on the upper surface, thus the conducting electrons and the polarizing electron density are spatially separated, offering insights into the fundamental mechanism of ferroelectric metallicity in these α-MXenes.

3.3. Photocatalytic applications of α-MXene

Hydrogen production through photocatalytic water splitting using semiconductor photocatalysts under sunlight represents one of the most promising green and renewable solutions to the depletion of fuel resources and the global greenhouse effect [12,54]. In recent years, to quickly achieve carbon peaking and carbon neutrality goals, the importance and urgency for synthesizing and developing an efficient photocatalyst with good catalytic activity for hydrogen production has reached an unprecedented height. Commonly, a suitable photocatalyst for water splitting should possess appropriate band edge levels to straddle the redox level of water, that is, the CBM need to be higher than reduction potential of H^+/H_2 (−4.44 eV), and the VBM must be lower than oxidation potential of O_2/H_2O (−5.67 eV) [55]. Hence, the theoretical minimum band gap for a semiconductor to be applied as photocatalysts is 1.23 eV. However, this band gap has overlooked the infrared part of the solar spectrum, which encompassed almost half of the solar energy. Fortunately, Yang et al. have proposed a new for hydrogen production mechanism by utilizing infrared light to break through the band gap restriction [56]. In this new mechanism, the restriction on the photocatalyst's band gap according to the following equation [56]:

$$E_g > 1.23 - \Delta\Phi, \quad (2)$$

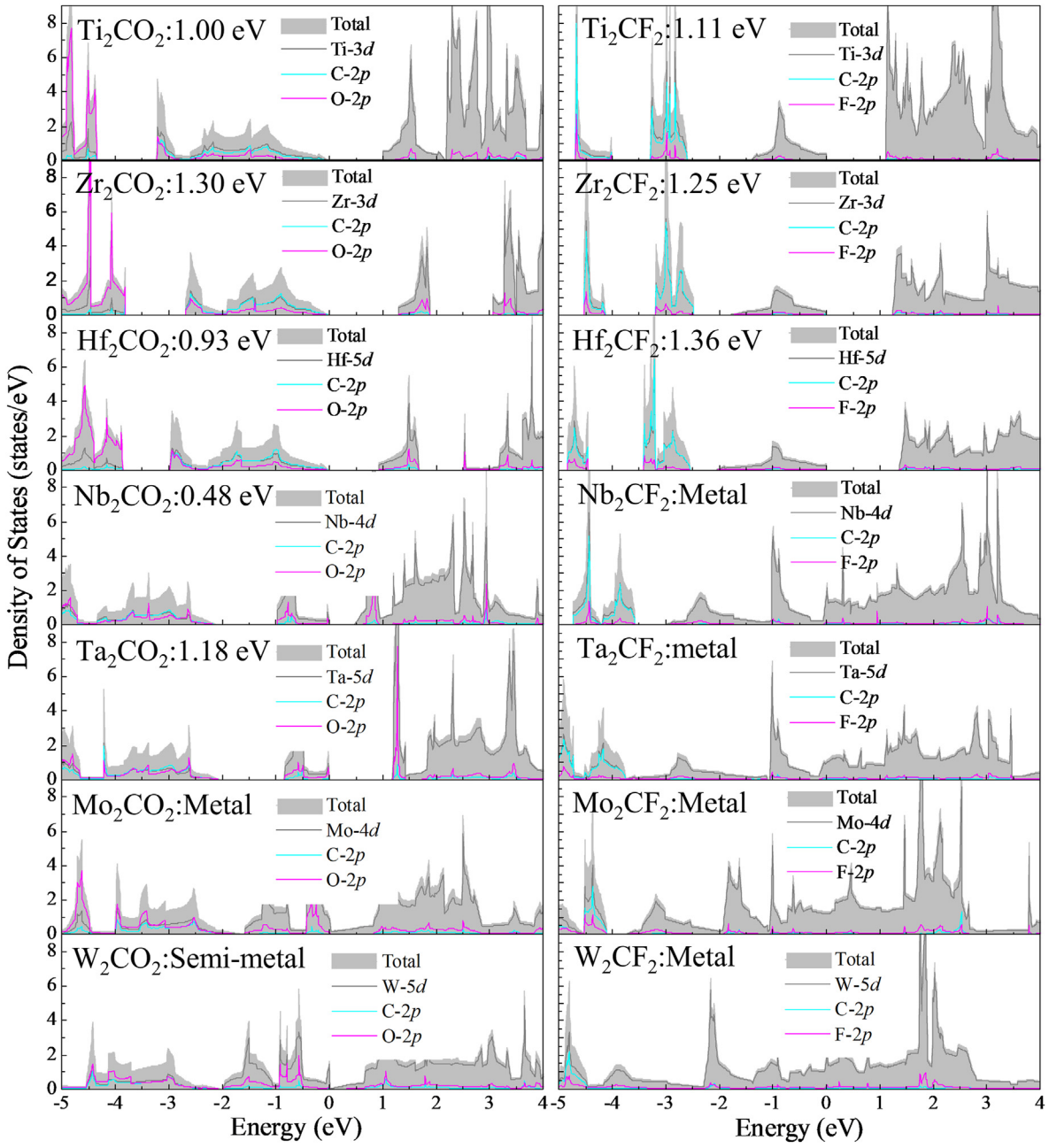

Fig. 4. Electronic structure of α-MXene. Calculated DOS and PDOS of M_2CX_2 (M = Ti, Zr, Hf, Nb, Ta, Mo, W; X = O and F) α-MXenes.

where $\Delta\Phi$ is the electrostatic potential difference between the top and bottom surfaces of the semiconductor photocatalyst. Hence, if the $\Delta\Phi$ is large enough, there is no restriction on the band gap. Meanwhile, a moderate value of $\Delta\Phi$ can reduce the band gap of the photocatalyst into the infrared wavelength. The key issue for this proposed model is to search a polar material with moderate intrinsic dipole. Another obstacle that a high-performance photocatalyst must overcome is the high rate of the photogenerated electron-hole recombination during the process of photocatalytic water splitting. While previous researches have elucidated that an out-of-plane built-in electric field induced by polar materials can enhance the dielectric screening potential and weaken the excitonic binding energy, which is beneficial for avoiding the recombination of photogenerated electrons and holes [57]. Notably, all the ferroelectric materials are in possession of piezoelectric or polar feature [58]. Hence, we speculated that our designed eight semiconductors α-MXenes may hold great potential as photocatalysts for water splitting, which not only can utilize visible or infrared solar radiation but also have effective separation of photogenerated electrons and holes.

To verify our hypothesis, we have firstly calculated the electrostatic potential difference $\Delta\Phi$, as listed in Table S3, from which one can see that various electrostatic potential differences are expected. The examined $\Delta\Phi$ are 2.23 eV, 1.11 eV, 2.01 eV, 0.11 eV, 3.13 eV, 0.25 eV, 1.01 eV, and 1.08 eV for Ti_2CO_2, Ti_2CF_2, Zr_2CO_2, Zr_2CF_2, Hf_2CO_2, Hf_2CF_2, Nb_2CO_2, and Ta_2CO_2, respectively. Thus, these eight α-MXenes are promising candidates to match the new photocatalytic mechanism. Furthermore, to verify the photocatalytic activity and favorable band edge positions, the energy alignments of VBM and CBM considering electrostatic potential difference are estimated and shown in Fig. 6a–c and Fig. S5. The estimated ΔE_R and ΔE_O in Table S3 are respective gained by CBM minus water reduction potential and water oxidation potential minus VBM. It is found that, for Ti_2CO_2, Hf_2CO_2, and Ta_2CO_2, the energy level of CBM lies below the oxidation potential of water with the VBM level locating above

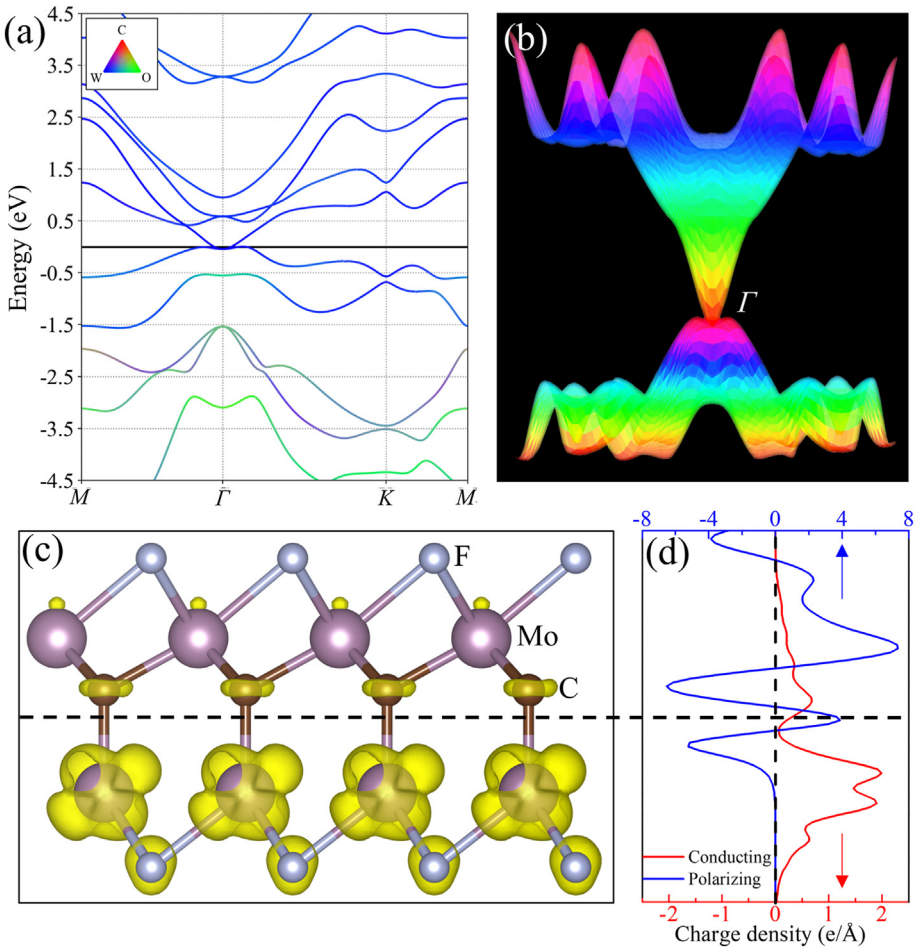

Fig. 5. Ferroelectric (semi)metallicity in α-MXene. (a) Calculated band structure and (b) three-dimension band profile around the Fermi level of W_2CO_2 α-MXene. (c) Partial electron density within an energy range of ±0.05 eV around the Fermi level of Mo_2CF_2. (d) The estimated conducting electron density (red lines) and polarizing electron density (blue lines) of Mo_2CF_2.

the reduction potential of water, suggesting the appropriate band edge alignments. Moreover, especially for Ti_2CO_2, the ΔE_R and ΔE_O can reach as high as 1.30 eV and 0.70 eV, implying its high power to drive electrons for reduction reaction and holes for oxidation reactions during dissociating process, respectively. For Ti_2CF_2, Zr_2CO_2 Zr_2CF_2, Hf_2CO_2, and Nb_2CO_2, the VBM levels are located inside the water oxidation, as illustrated in Fig. S5, thus cannot provide enough driving force for producing O_2. Noticeably, the band gaps of Ti_2CO_2, and Ta_2CO_2 are smaller than 1.23 eV, which preliminarily implies that our previous hypothesis are feasible.

Thereafter, we have calculated the optical absorption spectra by HSE06-TDHF approach to evaluate the utilization of solar energy for Ti_2CO_2, Hf_2CO_2, and Ta_2CO_2. As presented in Fig. 6d, all three α-MXenes exhibit substantially large optical absorption under visible and ultraviolet range. In this range, the absorption coefficients can reach as high as 6×10^5 cm^{-1}. The absorbance of bulk silicon is also plotted for reference comparison [59]. In contrast to silicon and numerous other 2D materials [60], where light absorbance drops sharply in the visible-light wavelength range, these three α-MXenes show significant light absorption across the entire visible-light spectrum. Note that Ta_2CO_2 shows the highest solar energy utilization of the three semiconductor photocatalysts almost in all the explored optical region. Significantly, the optical absorption coefficients for Ta_2CO_2 are still up to 10^5 cm^{-1} level in the infrared light region, which account for nearly half of solar spectrum. Such results are powerful evidence that our new designed α-MXenes not only have abundant harvest in visible and ultraviolet region but also exhibit outstanding light absorption abilities from infrared light, which confirmed our previous hypothesis.

As expounded before, our proposed α-MXenes are ferroelectric materials, hence the intrinsic dipole is induced, finally leading to an internal electric field in these structures. When the photocatalytic reactions are set off, the photo electrons and holes are generated and separated. Meanwhile, the electric field in α-MXenes can serve as an auxiliary booster to break up an exciton pair, thus the photo-excited electrons will transport to the one side of the layered structure for hydrogen generation, and holes diffuse to the other side to produce oxygen. As the band structure and band decomposed displayed in Fig. 6e, f, and g, upon absorption of light, the electrons and holes populate on the lower and upper zone of these three α-MXenes, respectively. As a result, the water reduction and oxidation occur on opposite areas of the layered α-MXenes, which is beneficail for not only efficient separations of photo-generated electrons and holes but also spatial generations of hydrogen and oxygen gas. We have then evaluated hydrogen evolution reaction (HER) and oxygen evolution reaction (OER) on both upper and lower surfaces of α-MXenes for a deeply understanding, the results are plotted in Fig. 6e, f, and g. We can see that, for all the three explored structures, the Gibbs free energy differences (ΔG_{H^*}) on lower surfaces are smaller than those on upper surfaces. That is, HER reactions are most likely to occur on the lower region of the structures, which align well with our previous analysis. In addition, under the potential provided by photoinduced electrons indicated in Fig. 6a, b, and c, the HER can proceed upon light irradiation. We then investigated the other half-reaction of water oxidation of these three α-MXenes. The species of OH*, O*, OOH*, and O_2 are the intermediates and final products of the OER process, respectively. It can be

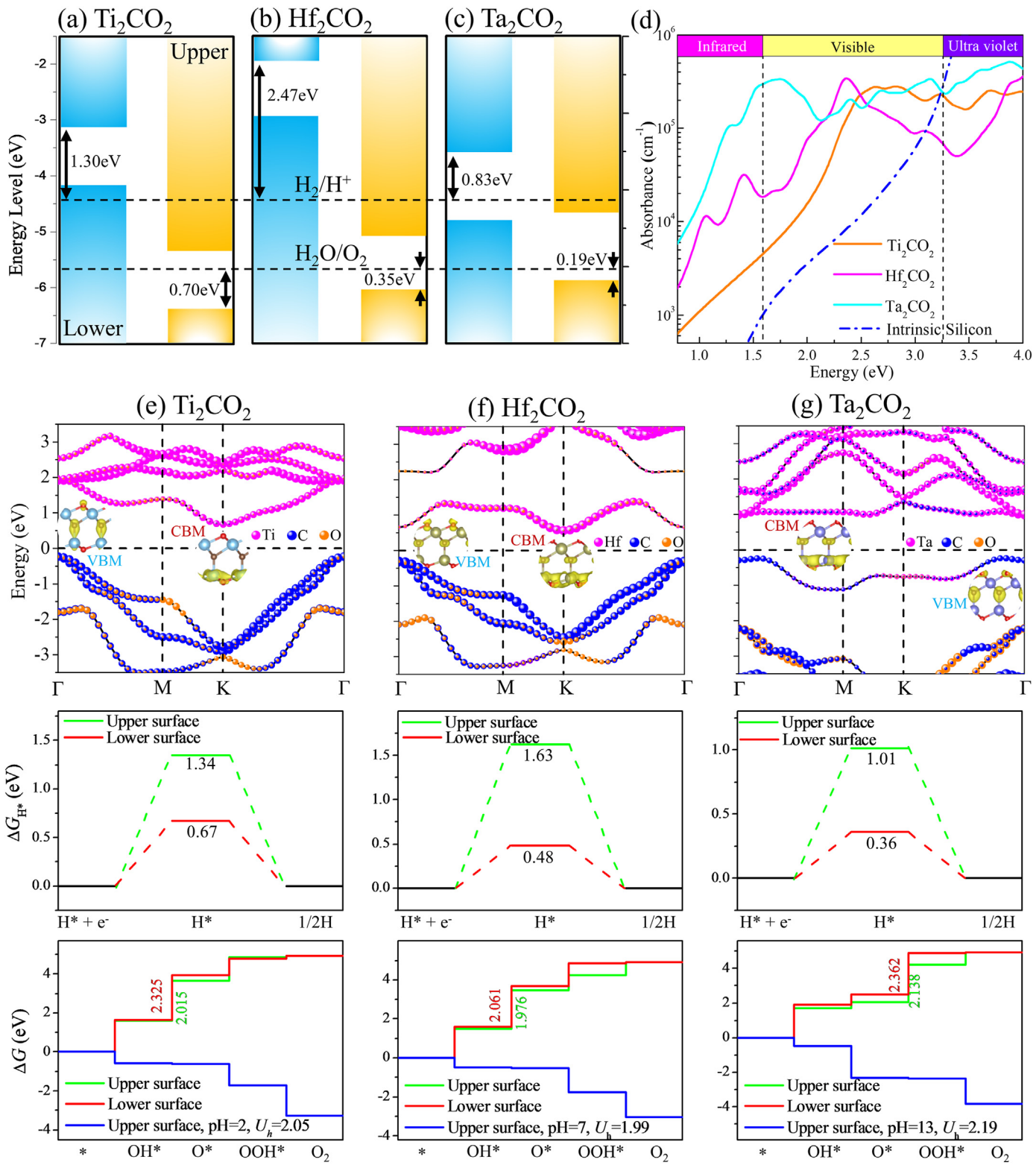

Fig. 6. Photocatalysis properties of α-MXenes. Electronic band alignment of (a) Ti_2CO_2, (b) Hf_2CO_2, and (c) Ta_2CO_2 with relative to the water redox potentials. The redox potentials of water are denoted as the black dashed line. (d) Optical absorption spectra of Ti_2CO_2, Hf_2CO_2, and Ta_2CO_2 by the HSE06-TDHF functional. The HSE06 band structures with band decomposed charge distribution for the CBM and VBM, free energy diagrams for HER on the upper and lower surface, and OER on the upper and lower surface of (e) Ti_2CO_2, (f) Hf_2CO_2, and (g) Ta_2CO_2, respectively.

observed that for Ti_2CO_2 and Hf_2CO_2, the formation of intermediate O* represents the rate-limiting steps, whereas for Ta_2CO_2, the formation of OOH* intermediate serves as the rate-limiting steps. Evidently, the OER reactions occur more readily on the upper surfaces for the three α-MXenes, as these surfaces exhibit lower activation energies for the rate-limiting steps. Such results are completely consistent with our previous expectations that hydrogen and oxygen gas can be generated locationally from two opposite surfaces of the two-dimensional materials.

Furthermore, when these three α-MXenes are subjected to light irradiation, the photoexcited holes create external potentials (U_h) as $U_h = \Delta E_O + 1.23 + pH \times 0.059$. For Ti_2CO_2, when the pH of the solution reaches 2, the external potential can achieve to 2.05 eV. Hence, all the OER reaction steps exhibit a downward trend, demonstrating that O_2 can produce spontaneously when pH > 2. For Hf_2CO_2 and Ta_2CO_2, the pH values for OER process occurring simultaneously are 7 and 13, respectively. It is can be concluded that these three materials can be used in various acidic and

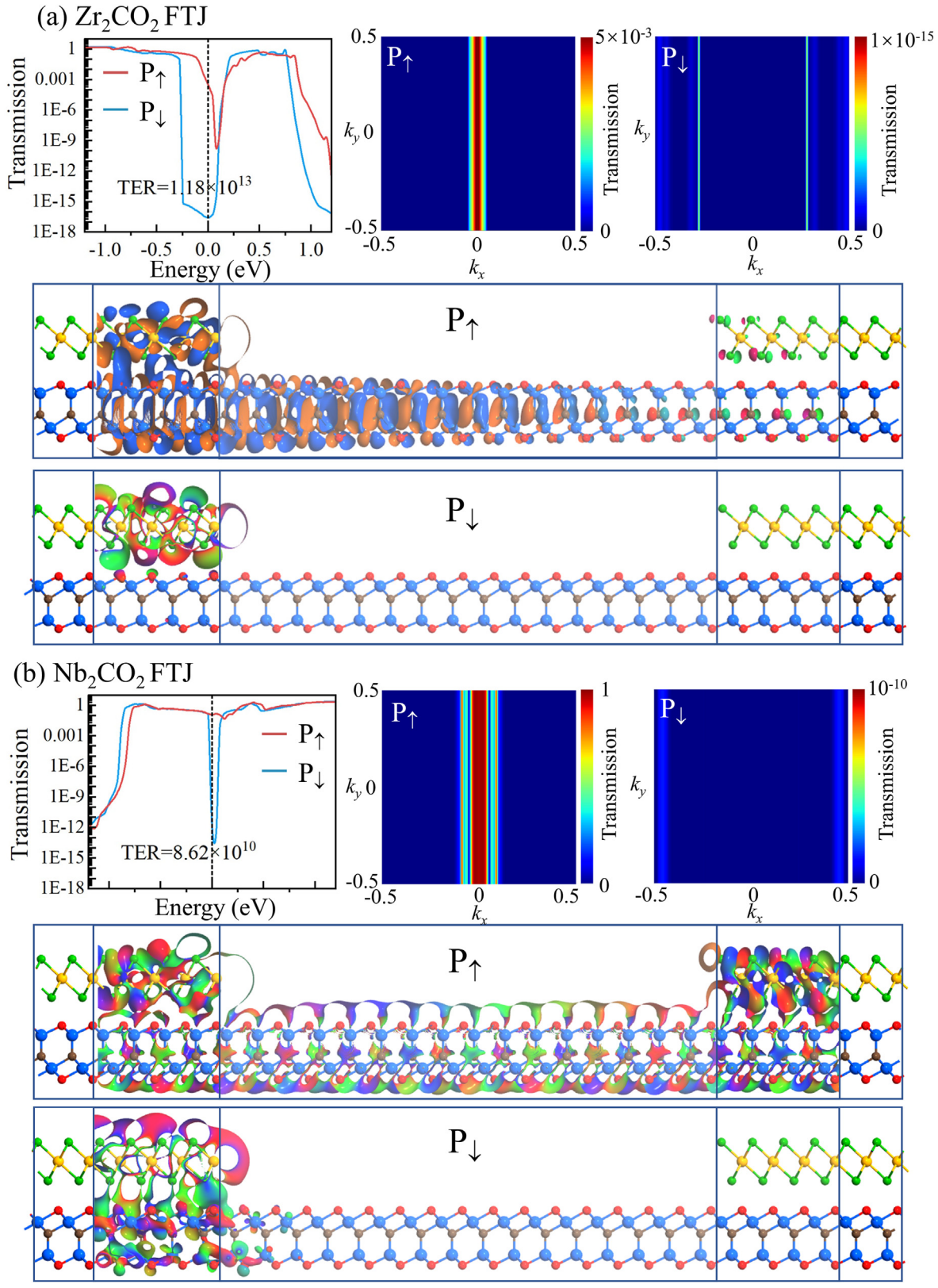

Fig. 7. Spintronic properties of α-MXenes. The transmission curves (top-left part) and spectrums (top-right part), as well as the transmission eigenstates (bottom part) of the (a) Zr_2CO_2-based and (b) Nb_2CO_2-based FTJs.

alkaline environments to meet different oxygen production requirements. In summary, the ferroelectric property of α-MXenes make them efficient photocatalysts for splitting water into hydrogen and oxygen.

3.4. Spintronic applications of α-MXene

Among various 2D materials, 2D ferroelectric materials have captured increasing research interest due to the spontaneous electric polarization [61,62]. Compared with three-dimensional (3D) perovskite ferroelectric materials, these 2D ferroelectric materials can hold their ferroelectric properties when the thickness is reduced to the single-layer limit [63,64]. These materials exhibit two distinct ferroelectric states that can be toggled using an external electric field, a characteristic of significant importance in practical applications. Indeed, the property that two distinct ferroelectric states can be regarded as "0" and "1" states in binary storage, which is suitable for applying in nonvolatile memory devices, such as FTJs [65–67]. The recent theoretical investigations on a lateral 2D FTJ composed of graphene and ferroelectric α-In_2Se_3 have demonstrated an impressive tunneling electroresistance ratio of approximately 1×10^8 %. This finding highlights the potential of such FTJ in the development of ferroelectric memory devices [68]. However, the study of integrating ferroelectrics into devices is still in its infancy, the search for new 2D ferroelectrics with exceptional device performance remains a pressing task. Due to the similar atomic stackings to α-In_2Se_3, our designed α-MXenes may endow with huge potential of novel applications in spintronics. To investigate their possible application of α-MXenes for the ferroelectric memory devices, we have constructed $X_2CO_2/MoSe_2$ (X = Nb, Zr)-based FTJs to study the electronic transport properties. The spin-dependent conductance of the tunnel junction per unit cell area is calculated by [69].

$$G(E) = \frac{2e^2}{h} T(E), \tag{3}$$

where $T(E) = \sum_{k_\parallel} T(k_\parallel, E)$ is the k-point averaged transmission function at energy E and $T(k_\parallel, E)$ is the k resolved transmission function with $k_\parallel = k_x$. The tunnel electroresistance (TER) ratio is calculated by the formula [70]

$$\mathrm{TER} = \frac{|G_\uparrow - G_\downarrow|}{\min(G_\uparrow, G_\downarrow)}, \tag{4}$$

where $G_\uparrow$ and $G_\downarrow$ are the tunneling conductances of the FTJs when the ferroelectric layer is in the up-polarized and down-polarized states, respectively.

Herein, 1T-$MoSe_2/X_2CO_2$ (X = Nb, Zr) heterostructures are utilized as electrodes. Various configurations of $X_2CO_2/MoSe_2$ heterostructures are considered to determine the most stable configurations, as shown in Fig. S6. Total energies of $X_2CO_2/MoSe_2$ heterostructures with different configurations are summarized in Table S4. Obviously, the most stable stacking configurations for $Zr_2CO_2/MoSe_2$ and $Nb_2CO_2/MoSe_2$ heterostructures are type IV from Table S4. We further construct the FTJs based on these most stable stacking configurations, as depicted in Fig. S7. To explore their electronic transport properties, the transmission curves and spectrums of the FTJs from −1.2 eV to 1.2 eV, as well as the transmission eigenstates of corresponding highest transmission areas are calculated and plotted in Fig. 7a and b. As is shown, for Zr_2CO_2-based FTJ, the $P_\uparrow$ and $P_\downarrow$ transmission curves are almost coincided in the low energy region (less than 0.3 eV). Both $P_\uparrow$ and $P_\downarrow$ transmission curves exhibit a rapid decline around the Fermi level and high energy region (greater than 0.7 eV). The $P_\uparrow$ and $P_\downarrow$ transmission coefficients of these FTJs show a considerable difference at the Fermi level, which could result in an apparent TER effect. The calculated TER ratio is 1.18×10^{13} for Zr_2CO_2-based FTJ. Such huge TER ratio of both FTJs reveals that these FTJs show an excellent application for ferroelectric memory devices. The transmission spectrum of $P_\uparrow$ state for Zr_2CO_2-based FTJ is located at $k_x = 0$, whereas that of $P_\downarrow$ is mainly located around $k_x = 0.26$. As a result, the transmission spectrums between different polarization states also show remarkable differences, which also reveals the origin of TER effect. For Nb_2CO_2-based FTJ, the $P_\uparrow$ and $P_\downarrow$ transmission curves are nearly aligned throughout the entire energy range, except in the vicinity of the Fermi level. The $P_\uparrow$ transmission curve exhibits little change around the Fermi level and remains at a relatively high level, whereas the $P_\downarrow$ transmission curve exhibits a sharp decline followed by a rise. The calculated TER ratios are 8.62×10^{10} for Nb_2CO_2-based FTJ. In addition, the transmission spectrum of $P_\uparrow$ state for Nb_2CO_2-based FTJ shows that the transmission area is mainly located around $k_x = 0$, while the transmission spectrum of $P_\downarrow$ state for Nb_2CO_2-based FTJ is mainly located around $k_x = 0.44$. Furthermore, the transmission eigenstates of corresponding highest transmission area for both FTJs show that the transmission eigenstates of FTJ in $P_\downarrow$ state fill the whole FTJ, which are much higher than that of $P_\uparrow$ state. In summary, Zr_2CO_2 and Nb_2CO_2-based FTJs exhibit high TER ratios, emphasizing their potential for use in advanced ferroelectric memory devices.

4. Conclusions

In conclusion, based on first-principles computations, we have discovered a new series of 2D ferroelectric materials with the composition M_2CO_2 from the MXene family. This phase is derived from the previously explored hexagonal MXene phase, and is named as α-MXenes due to the similar atomic configurations to α-In_2Se_3. Firstly, the stabilities of these α-MXenes have been identified through phonon and formation energy calculations. Moreover, α-MXenes exhibit a range of electric polarization and polarization reversal energy barrier from 0.008 eÅ to 0.156 eÅ and 0.496eV to 1.941 eV, respectively. Interestingly, W_2CO_2 α-MXene is an intrinsic Dirac-semimetal material, and Nb_2CF_2, Ta_2CF_2, Mo_2CO_2, Mo_2CF_2, and W_2CF_2 α-MXenes have been proved to be rare ferroelectric metal by our calculations. We have theoretically concluded that Ti_2CO_2, Hf_2CO_2, Ta_2CO_2 α-MXenes are promising photocatalysts for water splitting. Particularly, they can overcome the fundamental restriction of the band gap, thereby extending the optical absorption range into the visible and near-infrared region. Due to the internal electric field induced by ferroelectric effect, these three α-MXenes demonstrate superior separation of free electrons and holes, which greatly benefits the facilitation of the photocatalytic process. Notably, α-MXenes Zr_2CO_2 and Nb_2CO_2-based FTJs demonstrate an excellent performance, with the evaluated TER ratios of 1.18×10^{13} and 8.62×10^{10}, respectively, highlighting their strong potential for applications in advanced ferroelectric memory devices. Our comprehensive study not only predicts a new ferroelectric MXene phase and uncover innovative physical characteristics but also explores underlying applications in the fields of photocatalysis and spintronics.

CRediT authorship contribution statement

Yinggan Zhang: Writing – review & editing, Writing – original draft, Visualization, Investigation, Formal analysis, Data curation. **Zhou Cui:** Investigation, Formal analysis, Data curation. **Baisheng Sa:** Writing – review & editing, Supervision. **Jian Zhou:** Writing – review & editing, Supervision, Conceptualization. **Zhimei Sun:** Writing – review & editing, Supervision, Resources, Conceptualization.

Declaration of competing interest

The authors declare that they have no known competing financial interests or personal relationships that could have appeared to influence the work reported in this paper.

Acknowledgements

This work was supported by the National Key Research and Development Program of China (2022YFB3807200), and the National Natural Science Foundation of China (52201022).

Appendix A. Supplementary data

Supplementary data to this article can be found online at https://doi.org/10.1016/j.tramat.2025.100004.

References

[1] K.S. Novoselov, A.K. Geim, S.V. Morozov, D. Jiang, Y. Zhang, S.V. Dubonos, I.V. Grigorieva, A.A. Firsov, Electric field effect in atomically thin carbon films, Science 306 (2004) 666–669, https://doi.org/10.1126/science.1102896.

[2] G.R. Bhimanapati, Z. Lin, V. Meunier, Y. Jung, J. Cha, S. Das, D. Xiao, Y. Son, M.S. Strano, V.R. Cooper, Recent advances in two-dimensional materials beyond graphene, ACS Nano 9 (2015) 11509–11539, https://doi.org/10.1021/acsnano.5b05556.

[3] F. Shahzad, M. Alhabeb, C.B. Hatter, B. Anasori, S.M. Hong, C.M. Koo, Y. Gogotsi, Electromagnetic interference shielding with 2D transition metal carbides (MXenes), Science 353 (2016) 1137–1140, https://doi.org/10.1126/science.aag2421.

[4] A. VahidMohammadi, J. Rosen, Y. Gogotsi, The world of two-dimensional carbides and nitrides (MXenes), Science 372 (2021) eabf1581, https://doi.org/10.1126/science.abf1581.

[5] A.D. Handoko, S.N. Steinmann, Z.W. Seh, Theory-guided materials design: two-dimensional MXenes in electro- and photocatalysis, Nanoscale Horiz 4 (2019) 809–827, https://doi.org/10.1039/c9nh00100j.

[6] X. Zhan, C. Si, J. Zhou, Z. Sun, MXene and MXene-based composites: synthesis, properties and environment-related applications, Nanoscale Horiz 5 (2020) 235–258, https://doi.org/10.1039/c9nh00571d.

[7] P. Xiong, B. Sun, N. Sakai, R. Ma, T. Sasaki, S. Wang, J. Zhang, G. Wang, 2D superlattices for efficient energy storage and conversion, Adv. Mater. 32 (2019) 1902654, https://doi.org/10.1002/adma.201902654.

[8] Y. Xia, T.S. Mathis, M.Q. Zhao, B. Anasori, A. Dang, Z.H. Zhou, H. Cho, Y. Gogotsi, S. Yang, Thickness-independent capacitance of vertically aligned liquid-crystalline MXenes, Nature 557 (2018) 409–412, https://doi.org/10.1038/s41586-018-0109-z.

[9] M.R. Lukatskaya, O. Mashtalir, C.E. Ren, Y. Dall'Agnese, P. Rozier, P.L. Taberna, M. Naguib, P. Simon, M.W. Barsoum, Y. Gogotsi, Cation intercalation and high volumetric capacitance of two-dimensional titanium carbide, Science 341 (2013) 1502–1505, https://doi.org/10.1126/science.124148.

[10] Y. Wang, X. Yu, S. Xu, J. Bai, R. Xiao, Y.-S. Hu, H. Li, X.-Q. Yang, L. Chen, X. Huang, A zero-strain layered metal oxide as the negative electrode for long-life sodium-ion batteries, Nat. Commun. 4 (2013) 2365, https://doi.org/10.1038/ncomms3365.

[11] Z. Guo, J. Zhou, L. Zhu, Z. Sun, MXene: a promising photocatalyst for water splitting, J. Mater. Chem. A 4 (2016) 11446–11452, https://doi.org/10.1039/c6ta04414j.

[12] C.-F. Fu, X. Li, Q. Luo, J. Yang, Two-dimensional multilayer M_2CO_2 (M=Sc, Zr, Hf) as photocatalysts for hydrogen production from water splitting: a first principles study, J. Mater. Chem. A 5 (2017) 24972–24980, https://doi.org/10.1039/c7ta08812d.

[13] H. Zhang, G. Yang, X. Zuo, H. Tang, Q. Yang, G. Li, Computational studies on the structural, electronic and optical properties of graphene-like MXenes (M_2CT_2, M= Ti, Zr, Hf; T= O, F, OH) and their potential applications as visible-light driven photocatalysts, J. Mater. Chem. A 4 (2016) 12913–12920, https://doi.org/10.1039/c6ta04628b.

[14] A. Chandrasekaran, A. Mishra, A.K. Singh, Ferroelectricity, antiferroelectricity, and ultrathin 2D electron/hole gas in multifunctional monolayer MXene, Nano Lett. 17 (2017) 3290–3296, https://doi.org/10.1021/acs.nanolett.7b01035.

[15] L. Zhang, C. Tang, C. Zhang, A. Du, First-principles screening of novel ferroelectric MXene phases with a large piezoelectric response and unusual auxeticity, Nanoscale 12 (2020) 21291–21298, https://doi.org/10.1039/d0nr06609e.

[16] D. Wijethunge, L. Zhang, A. Du, Prediction of two-dimensional ferroelectric metal MXenes, J. Mater. Chem. C 9 (2021) 11343–11348, https://doi.org/10.1039/d1tc02213j.

[17] M. Khazaei, M. Arai, T. Sasaki, C.Y. Chung, N.S. Venkataramanan, M. Estili, Y. Sakka, Y. Kawazoe, Novel electronic and magnetic properties of two-dimensional transition metal carbides and nitrides, Adv. Funct. Mater. 23 (2013) 2185–2192, https://doi.org/10.1002/adfm.201202502.

[18] Y. Zhang, Z. Cui, B. Sa, N. Miao, J. Zhou, Z. Sun, Computational design of double transition metal MXenes with intrinsic magnetic properties, Nanoscale Horiz 7 (2022) 276–287, https://doi.org/10.1039/D1NH00621E.

[19] Y. Zhang, B. Sa, N. Miao, J. Zhou, Z. Sun, Computational mining of Janus Sc_2C-based MXenes for spintronic, photocatalytic, and solar cell applications, J. Mater. Chem. A 9 (2021) 10882–10892, https://doi.org/10.1039/d1ta00614b.

[20] W. Ding, J. Zhu, Z. Wang, Y. Gao, D. Xiao, Y. Gu, Z. Zhang, W. Zhu, Prediction of intrinsic two-dimensional ferroelectrics in In_2Se_3 and other III_2-VI_3 van der Waals materials, Nat. Commun. 8 (2017) 14956, https://doi.org/10.1038/ncomms14956.

[21] C.K.Y. Tan, W. Fu, K.P. Loh, Polymorphism and ferroelectricity in indium(III) selenide, Chem. Rev. 123 (2023) 8701–8717, https://doi.org/10.1021/acs.chemrev.3c00129.

[22] Y. Zhou, D. Wu, Y. Zhu, Y. Cho, Q. He, X. Yang, K. Herrera, Z. Chu, Y. Han, M.C. Downer, H. Peng, K. Lai, Out-of-plane piezoelectricity and ferroelectricity in layered α-In_2Se_3 nanoflakes, Nano Lett. 17 (2017) 5508–5513, https://doi.org/10.1021/acs.nanolett.7b02198.

[23] C. Zheng, L. Yu, L. Zhu, J.L. Collins, D. Kim, Y. Lou, C. Xu, M. Li, Z. Wei, Y. Zhang, Room temperature in-plane ferroelectricity in van der Waals In_2Se_3, Sci. Adv. 4 (2018) eaar7720, https://doi.org/10.1126/sciadv.aar7720.

[24] Y.T. Huang, N.K. Chen, Z.Z. Li, X.P. Wang, H.B. Sun, S. Zhang, X.B. Li, Two-dimensional In_2Se_3: a rising advanced material for ferroelectric data storage, InfoMat 4 (2022) e12341, https://doi.org/10.1002/inf2.12341.

[25] Y. Yang, L. Zhang, J. Chen, X. Zheng, L. Zhang, L. Xiao, S. Jia, An electrically switchable anti-ferroelectric bilayer In_2Se_3 based opto-spintronic device, Nanoscale 13 (2021) 8555–8561, https://doi.org/10.1039/d1nr00369k.

[26] G. Kresse, J. Furthmüller, Efficient iterative schemes for ab initio total-energy calculations using a plane-wave basis set, Phys. Rev. B 54 (1996) 11169, https://doi.org/10.1103/PhysRevB.54.11169.

[27] G. Kresse, D. Joubert, From ultrasoft pseudopotentials to the projector augmented-wave method, Phys. Rev. B 59 (1999) 1758, https://doi.org/10.1103/PhysRevB.59.1758.

[28] G. Wang, L. Peng, K. Li, L. Zhu, J. Zhou, N. Miao, Z. Sun, ALKEMIE: an intelligent computational platform for accelerating materials discovery and design, Comput. Mater. Sci. 186 (2021) 110064, https://doi.org/10.1016/j.commatsci.2020.110064.

[29] G. Wang, K. Li, L. Peng, Y. Zhang, J. Zhou, Z. Sun, High-throughput automatic integrated material calculations and data management intelligent platform and the application in novel alloys, Acta Metall. Sin. 58 (2022) 75–88, https://doi.org/10.11900/0412.1961.2021.00041.

[30] J.P. Perdew, K. Burke, M. Ernzerhof, Generalized gradient approximation made simple, Phys. Rev. Lett. 77 (1996) 3865, https://doi.org/10.1103/PhysRevLett.77.3865.

[31] L. Bengtsson, Dipole correction for surface supercell calculations, Phys. Rev. B 59 (1999) 12301, https://doi.org/10.1103/PhysRevB.59.12301.

[32] F. Furche, R. Ahlrichs, Adiabatic time-dependent density functional methods for excited state properties, J. Chem. Phys. 117 (2002) 7433–7447, https://doi.org/10.1063/1.1508368.

[33] M. Marsman, J. Paier, A. Stroppa, G. Kresse, Hybrid functionals applied to extended systems, J. Phys. Condens. Matter 20 (2008) 064201, https://doi.org/10.1088/0953-8984/20/6/064201.

[34] A. Togo, F. Oba, I. Tanaka, First-principles calculations of the ferroelastic transition between rutile-type and $CaCl_2$-type SiO_2 at high pressures, Phys. Rev. B 78 (2008) 134106, https://doi.org/10.1103/PhysRevB.78.134106.

[35] X. Gonze, C. Lee, Dynamical matrices, Born effective charges, dielectric permittivity tensors, and interatomic force constants from density-functional perturbation theory, Phys. Rev. B 55 (1997) 10355, https://doi.org/10.1103/PhysRevB.55.10355.

[36] M. Brandbyge, J.L. Mozos, P. Ordejón, J. Taylor, K. Stokbro, Density-functional method for nonequilibrium electron transport, Phys. Rev. B 65 (2002) 165401, https://doi.org/10.1103/PhysRevB.65.165401.

[37] S. Smidstrup, T. Markussen, P. Vancraeyveld, J. Wellendorff, J. Schneider, T. Gunst, B. Verstichel, D. Stradi, P.A. Khomyakov, U.G. Vej-Hansen, M.E. Lee, S.T. Chill, F. Rasmussen, G. Penazzi, F. Corsetti, A. Ojanpera, K. Jensen, M.L.N. Palsgaard, U. Martinez, A. Blom, M. Brandbyge, K. Stokbro, QuantumATK: an integrated platform of electronic and atomic-scale modelling tools, J. Phys. Condens. Matter 32 (2020) 015901, https://doi.org/10.1088/1361-648X/ab4007.

[38] M.J. van Setten, M. Giantomassi, E. Bousquet, M.J. Verstraete, D.R. Hamann, X. Gonze, G.M. Rignanese, The PseudoDojo: training and grading a 85 element optimized norm-conserving pseudopotential table, Comput. Phys. Commun. 226 (2018) 39–54, https://doi.org/10.1016/j.cpc.2018.01.012.

[39] V. Blum, R. Gehrke, F. Hanke, P. Havu, V. Havu, X. Ren, K. Reuter, M. Scheffler, Ab initio molecular simulations with numeric atom-centered orbitals, Comput. Phys. Commun. 180 (2009) 2175–2196, https://doi.org/10.1016/j.cpc.2009.06.022.

[40] C. Cui, W.-J. Hu, X. Yan, C. Addiego, W. Gao, Y. Wang, Z. Wang, L. Li, Y. Cheng, P. Li, Intercorrelated in-plane and out-of-plane ferroelectricity in ultrathin two-dimensional layered semiconductor In_2Se_3, Nano Lett. 18 (2018) 1253–1258, https://doi.org/10.1021/acs.nanolett.7b04852.

[41] C. Huang, J. Zhou, H. Sun, F. Wu, Y. Hou, E. Kan, Toward room-temperature electrical control of magnetic order in multiferroic van der Waals materials, Nano Lett. 22 (2022) 5191–5197, https://doi.org/10.1021/acs.nanolett.2c00930.

[42] J. He, P. Lyu, L.Z. Sun, Á. Morales García, P. Nachtigall, High temperature spin-polarized semiconductivity with zero magnetization in two-dimensional Janus MXenes, J. Mater. Chem. C 4 (2016) 6500–6509, https://doi.org/10.1039/C6TC01287F.

[43] T. Jungwirth, X. Marti, P. Wadley, J. Wunderlich, Antiferromagnetic spintronics, Nat. Nanotechnol. 11 (2016) 231–241, https://doi.org/10.1038/nnano.2016.18.

[44] I. Ismail, R.a.S. Azis, A review of magnetic nanocomposites for EMI shielding: synthesis, properties, and mechanisms, J. Mater. Sci. 59 (2024) 5293–5329, https://doi.org/10.1007/s10853-024-09527-2.

[45] X.-H. Zha, J. Zhou, K. Luo, J. Lang, Q. Huang, X. Zhou, J.S. Francisco, J. He, S. Du, Controllable magnitude and anisotropy of the electrical conductivity of $Hf_3C_2O_2$ MXene, J. Phys. Condens. Matter 29 (2017) 165701, https://doi.org/10.1088/1361-648X/aa62da.

[46] Z. Liu, J. Liu, J. Zhao, YN_2 monolayer: novel p-state Dirac half metal for high-speed spintronics, Nano Res. 10 (2017) 1972–1979, https://doi.org/10.1007/s12274-016-1384-3.
[47] B. Sa, J. Zhou, Z. Sun, J. Tominaga, R. Ahuja, Topological insulating in GeTe/Sb_2Te_3 phase-change superlattice, Phys. Rev. Lett. 109 (2012) 096802, https://doi.org/10.1103/PhysRevLett.109.096802.
[48] M. Qi, C. An, Y. Zhou, H. Wu, B. Zhang, C. Chen, Y. Yuan, S. Wang, Y. Zhou, X. Chen, R. Zhang, Z. Yang, Pressure-driven Lifshitz transition in type-II Dirac semimetal $NiTe_2$, Phys. Rev. B 101 (2020) 115124, https://doi.org/10.1103/PhysRevB.101.115124.
[49] P.W. Anderson, E. Blount, Symmetry considerations on martensitic transformations: " ferroelectric" metals? Phys. Rev. Lett. 14 (1965) 217, https://doi.org/10.1126/science.1102896.
[50] W. Zhou, A. Ariando, Review on ferroelectric/polar metals, Jpn. J. Appl. Phys. 59 (2020) SI0802, https://doi.org/10.35848/1347-4065/ab8bbf.
[51] N.A. Benedek, T. Birol, 'Ferroelectric'metals reexamined: fundamental mechanisms and design considerations for new materials, J. Mater. Chem. C 4 (2016) 4000–4015, https://doi.org/10.1039/c5tc03856a.
[52] Z. Fei, W. Zhao, T.A. Palomaki, B. Sun, M.K. Miller, Z. Zhao, J. Yan, X. Xu, D.H. Cobden, Ferroelectric switching of a two-dimensional metal, Nature 560 (2018) 336–339, https://doi.org/10.1038/s41586-018-0336-3.
[53] X.-Y. Ma, H.-Y. Lyu, K.-R. Hao, Y.-M. Zhao, X. Qian, Q.-B. Yan, G. Su, Large family of two-dimensional ferroelectric metals discovered via machine learning, Science Bulletin 66 (2021) 233–242, https://doi.org/10.1016/j.scib.2020.09.010.
[54] Y. Zhang, B. Sa, J. Zhou, Z. Sun, Two-dimensional $(Zr_{0.5}Hf_{0.5})_2CO_2$: a promising visible light water-splitting photocatalyst with efficiently carrier separation, Comput. Mater. Sci. 186 (2021) 110013, https://doi.org/10.1016/j.commatsci.2020.110013.
[55] A.K. Singh, K. Mathew, H.L. Zhuang, R.G. Hennig, Computational screening of 2D materials for photocatalysis, J. Phys. Chem. Lett. 6 (2015) 1087–1098, https://doi.org/10.1021/jz502646d.
[56] X. Li, Z. Li, J. Yang, Proposed photosynthesis method for producing hydrogen from dissociated water molecules using incident near-infrared light, Phys. Rev. Lett. 112 (2014) 018301, https://doi.org/10.1103/PhysRevLett.112.018301.
[57] S. Zhang, H. Jin, C. Long, T. Wang, R. Peng, B. Huang, Y. Dai, MoSSe nanotube: a promising photocatalyst with an extremely long carrier lifetime, J. Mater. Chem. A 7 (2019) 7885–7890, https://doi.org/10.1039/c9ta00244h.
[58] R. Xiong, F. Xiao, J. Wen, H. Xiong, L. Jiang, Y. Qiu, C. Wen, B. Wu, B. Sa, Out-of-plane polarization modulated band alignments in β-In_2X_3/α-In_2X_3 (X= S and Se) vdW heterostructures, J. Phys. Condens. Matter 35 (2023) 485501, https://doi.org/10.1088/1361-648X/acf260.
[59] M.A. Green, M.J. Keevers, Optical properties of intrinsic silicon at 300 K, Prog. Photovoltaics Res. Appl. 3 (1995) 189–192, https://doi.org/10.1002/pip.4670030303.
[60] Q.H. Wang, K. Kalantar-Zadeh, A. Kis, J.N. Coleman, M.S. Strano, Electronics and optoelectronics of two-dimensional transition metal dichalcogenides, Nat. Nanotechnol. 7 (2012) 699, https://doi.org/10.1038/nnano.2012.193.
[61] Z. Guan, H. Hu, X. Shen, P. Xiang, N. Zhong, J. Chu, C. Duan, Recent progress in two-dimensional ferroelectric materials, Adv. Electron. Mater. 6 (2019) 1900818, https://doi.org/10.1002/aelm.201900818.
[62] L. Qi, S. Ruan, Y.J. Zeng, Review on recent developments in 2D ferroelectrics: theories and applications, Adv. Mater. 33 (2021) e2005098, https://doi.org/10.1002/adma.202005098.
[63] S. Yuan, X. Luo, H.L. Chan, C. Xiao, Y. Dai, M. Xie, J. Hao, Room-temperature ferroelectricity in $MoTe_2$ down to the atomic monolayer limit, Nat. Commun. 10 (2019) 1775, https://doi.org/10.1038/s41467-019-09669-x.
[64] C. Cui, F. Xue, W.-J. Hu, L.-J. Li, Two-dimensional materials with piezoelectric and ferroelectric functionalities, npj 2D Mater. Appl. 2 (2018) 18, https://doi.org/10.1038/s41699-018-0063-5.
[65] V. Garcia, M. Bibes, Ferroelectric tunnel junctions for information storage and processing, Nat. Commun. 5 (2014) 4289, https://doi.org/10.1038/ncomms5289.
[66] J. Ding, D.F. Shao, M. Li, L.W. Wen, E.Y. Tsymbal, Two-dimensional antiferroelectric tunnel junction, Phys. Rev. Lett. 126 (2021) 057601, https://doi.org/10.1103/PhysRevLett.126.057601.
[67] H. Bai, X. Li, H. Pan, P. He, Z.A. Xu, Y. Lu, Van der Waals antiferroelectric magnetic tunnel junction: a First-principles study of a $CrSe_2$/$CuInP_2S_6$/$CrSe_2$ junction, ACS Appl. Mater. Interfaces 13 (2021) 60200–60208, https://doi.org/10.1021/acsami.1c18949.
[68] L. Kang, P. Jiang, H. Hao, Y. Zhou, X. Zheng, L. Zhang, Z. Zeng, Giant tunneling electroresistance in two-dimensional ferroelectric tunnel junctions with out-of-plane ferroelectric polarization, Phys. Rev. B 101 (2020) 014105, https://doi.org/10.1103/PhysRevB.101.014105.
[69] R. Landauer, Electrical resistance of disordered one-dimensional lattices, Philos. Mag. 21 (2006) 863–867, https://doi.org/10.1080/14786437008238472.
[70] J.P. Velev, C.G. Duan, J.D. Burton, A. Smogunov, M.K. Niranjan, E. Tosatti, S.S. Jaswal, E.Y. Tsymbal, Magnetic tunnel junctions with ferroelectric barriers: prediction of four resistance states from first principles, Nano Lett. 9 (2009) 427–432, https://doi.org/10.1021/nl803318d.